DØ note 5369-CONF

Measurement of Triple Differential Photon Plus Jet Cross Section in $p\bar{p}$ Collisions at 1.96 TeV in DØ

The DØ Collaboration
URL: *http://www-d0.fnal.gov*
(Dated: March 14, 2007)

A measurement of the triple differential cross section for the process $p\bar{p} \rightarrow \gamma + jet + X$ is presented. This measurement is based on a data sample collected with an integrated luminosity of about 1.1 fb^{-1} between September 2002 − February 2006 by the DØ detector at the Fermilab Tevatron $p\bar{p}$ Collider running at $\sqrt{s}$ =1.96 TeV. The events selected for analysis contain photons with transverse momenta in the range of 30−300 GeV and pseudorapidities of $|\eta^{\gamma}|<1.0$ and a leading jet with transverse momentum $p_T > 15$ GeV. In these events, jet pseudorapidities are limited to lie within the ranges $|\eta^{jet}|<0.8$ or $1.5<|\eta^{jet}|<2.5$. The dependence of the cross section on the photon transverse momentum for different photon and jet rapidity regions is compared with the next-to-leading order QCD predictions using the CTEQ6.1M parameterizations of parton distribution functions.

Preliminary Results for Spring 2007 Conferences

I. INTRODUCTION

High energy $p\bar{p}$ collisions allow tests of QCD predictions at high values of transverse momenta (p_T). A comprehensive study of high-p_T jets [1] and isolated prompt photon events [2] performed at D0 using data collected during a previous Tevatron running period (Run I). The increased luminosity collected by the D0 Collaboration in the recent run (Run II) has resulted in a sizable sample of "$\gamma + jet$" events which allow high statistics QCD checks which were not possible with Run I statistics. The use of these events adds additional information to the results previously obtained in Run II from studies of high-p_T jets and prompt photon events [3, 4]. While the fundamental parton level subprocesses that define "$\gamma + jet$" events are the same as those that determine the inclusive isolated prompt photon production, with the "$\gamma + jet$" sample we also take into account the kinematics of the jets. The latter in association with the photon information sheds more light on the initial QCD dynamics.

An advantage of "$\gamma + jet$" events is that the isolated photons are mostly "direct" photons, i.e. those which are produced in some fundamental parton subprocesses. It is important to stress that these photons come unaltered from the parton subprocesses to the electromagnetic calorimeter. These subprocesses include: (1) the Compton-like partonic scattering $gq \to q\gamma$ which dominates in a wide kinematic range (see Fig. 1 below), and (2) the annihilation subprocess $q\bar{q} \to g\gamma$. The production cross section in the first case is obviously sensitive to a gluon density inside the colliding hadrons and, in principle, it may give an opportunity to tune the gluon distribution (see e.g. [7–9]) that still has noticeable uncertainties [10, 11].

A dominant source of background photons for "$\gamma^{dir} + jet$" events are the photons from hadron (π^0, η, *etc.*) decays and so called "fragmentation" photons [5]. The contribution from the parton-to-photon fragmentation mechanism is however suppressed after application of strong photon isolation criteria and it decreases as p_T^γ increases [6, 12].

This note presents the results of measurement of the triple differential cross section for $p\bar{p} \to \gamma + jet + X$ process in $p\bar{p}$ collisions at $\sqrt{s}$ =1.96 TeV with a photon located in the central pseudorapidity region of $|\eta^\gamma| < 1.0$ and a leading jet with $p_T > 15$ GeV in either the central ($|\eta^{jet}| < 0.8$) or the forward region ($1.5 < |\eta^{jet}| < 2.5$) [26]. The photon p_T range varies from 30 to 300 (200) GeV for the central (forward) jets. It should be noted that such events may include more than one jet. We denote the "leading" jet as the jet which has the largest p_T in the event. The differential cross sections for the $p\bar{p} \to \gamma + jet + X$ process was measured in the following four kinematic regions, differing by pseudorapidities of the leading jet and the most energetic photon:

Region 1: $(0.0<\eta^\gamma<1.0$ and $0.0<\eta^{jet}<0.8)$ or $(-1.0<\eta^\gamma<0.0$ and $-0.8<\eta^{jet}<0.0)$;
Region 2: $(0.0<\eta^\gamma<1.0$ and $-0.8<\eta^{jet}<0.0)$ or $(-1.0<\eta^\gamma<0.0$ and $0.0<\eta^{jet}<0.8)$;
Region 3: $(0.0<\eta^\gamma<1.0$ and $1.5<\eta^{jet}<2.5)$ or $(-1.0<\eta^\gamma<0.0$ and $-2.5<\eta^{jet}<-1.5)$;
Region 4: $(0.0<\eta^\gamma<1.0$ and $-2.5<\eta^{jet}<-1.5)$ or $(-1.0<\eta^\gamma<0.0$ and $1.5<\eta^{jet}<2.5)$.

The kinematic domain covered by these four regions and with the chosen p_T^γ range extends previous "γ+jet(s)" measurements [13–15].

Section II includes description of the selection criteria used to collect the $p\bar{p} \to \gamma + jet + X$ events, determination of signal event fractions (purities) and the dependence of the found purities on p_T^γ. In Section III we present the measured differential cross sections and compare with NLO QCD predictions. This comparison is done using the JETPHOX program [16] with the choice of CTEQ6.1M parametrization of parton distribution functions [11].

Figure 1 shows the estimate of the fractional contribution of $qg \to q\gamma$ subprocess to the associated production of a direct photon and a jet for different values of p_T^γ in the four kinematic regions described above. They are obtained with the two signal $2 \to 2$ subprocesses mentioned above used to simulate $p\bar{p} \to \gamma + jet + X$ events with the Monte Carlo event generator PYTHIA [17].

II. ANALYSIS

A. Selection Criteria.

Photon candidates were identified in the DØ detector [18] as isolated clusters of energy depositions in the uranium and liquid-argon sampling calorimeter. The electromagnetic (EM) section of the calorimeter is segmented longitudinally into four layers (EM1-EM4) of 2, 2, 7, and 10 radiation lengths respectively, and transversely into cells in pseudorapidity and azimuthal angle $\Delta\eta \times \Delta\phi = 0.1 \times 0.1$ (0.05×0.05 in EM3). In addition, the cluster may also contain the energy deposited in the hadronic portion of the calorimeter located behind the EM section [18].

To select photon candidates in data and Monte Carlo (MC) we have used the following criteria. Each EM cluster–photon candidate is formed by a simple cone algorithm with a cone size of $\mathcal{R} = \sqrt{\Delta\eta^2 + \Delta\phi^2} = 0.2$. The preselected events are required to pass one of the unprescaled EM triggers. The event vertex was required to be within 50 cm of

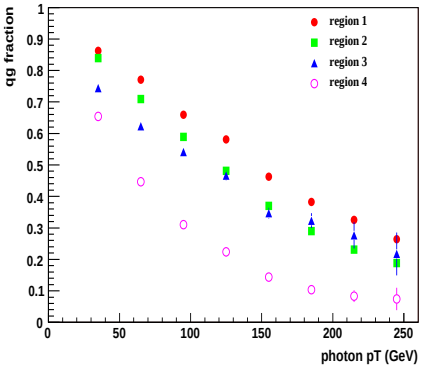

FIG. 1: PYTHIA simulation of the fractional contributions of $qg \to q\gamma$ subprocesses to the associated production of a direct photon and leading jet in the four kinematic regions.

the nominal center of the detector along the nominal beam axis ($|Z_{vtx}| < 50$ cm) and was required to have at least 3 associated tracks. Candidate EM clusters were accepted within the pseudorapidity region $|\eta| < 1.0$. To avoid inter-calorimeter boundaries and cracks, additional EM fiducial cuts we applied. The total geometric acceptance after these cuts was found to be 0.872 ± 0.005. Each candidate was required to deposit more than 96% of its detected energy in the EM section of the calorimeter and to satisfy isolation criteria in the angular region between $\mathcal{R} = 0.2$ and $\mathcal{R} = 0.4$ around the energy-weighted centroid: $Iso(\Delta\mathcal{R}02) < 0.07$. Here $Iso(\Delta\mathcal{R}02) = (EisoTot - EisoCore)/EisoCore$, where $EisoTot$ is the overall (EM+hadronic) tower energy in the (η, ϕ) cone of $\mathcal{R} = 0.4$ and $EisoCore$ is the EM tower energy in the cone of $\mathcal{R} = 0.2$. The probability to have any charged track spatially matched to the EM cluster in the event was required to be below 0.001. We also limit the energy weighted EM cluster width in the finely-segmented EM3 layer.The candidate photon was required to originate from the best primary vertex by fitting its location on the detector axis using the information obtained from the center-of-gravity of the EM cluster in the EM1-EM4 layers and of a cluster in the central preshower detector CPS. Events having anomalously large missing transverse energy were rejected by the cut $E_T^{miss} < 12.5 + 0.36\ p_T^{\gamma}$.

A set of additional three variables was used for further background suppression. They are 1) the number of cells that belong to the EM cluster, are in EM1, and have a cell energy $E_{cell} > 0.3$ GeV, 2) the fraction of the EM cluster energy deposited in the EM1 layer (just EM1 cells with energy $E_{cell} > 0.3$ GeV are considered), and 3) a scalar sum of track transverse momenta in the ring of $0.05 \leq \mathcal{R} \leq 0.4$ (with $p_T^{track} > 0.4$ GeV) around the photon direction. These variables turned out to be very efficient for background suppression and show consistent behavior for MC/data electrons from $Z \to ee$ events. They are used as an input to an artificial neural network (ANN) constructed for the photon selection using the JETNET package [19]. An additional cut on the single ANN output $O_{\rm NN} > 0.7$ is applied. The photon efficiency with respect to this cut is $0.93 - 0.97$ with a weak dependence on p_T^{γ}. The distributions of the ANN output for the MC direct photon, electromagnetic jets (EM-jets) from simulated QCD hadronic events and from data for $44 < p_T^{\gamma} < 50$ GeV are presented in Fig. 2.

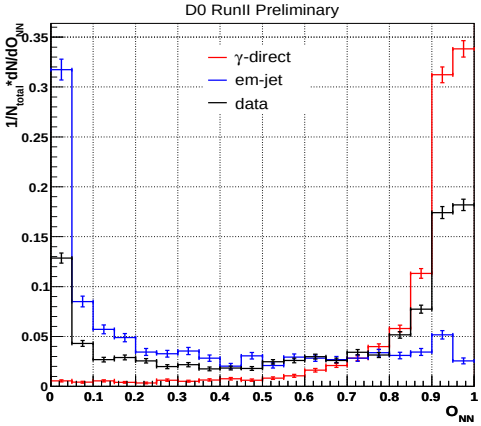

FIG. 2: Normalized distribution of ANN output for data, "$\gamma + jet$" signal and "$jet + jet$" background events for $44 < p_T^{\gamma} < 50$ GeV after application of the main selection criteria.

The total photon selection efficiency is presented in Fig. 3. The overall systematic uncertainty of the photon

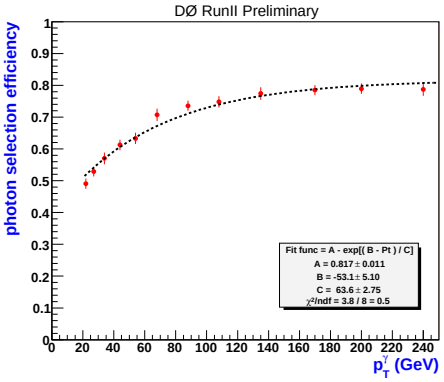

FIG. 3: The photon selection efficiency as a function of p_T.

selection criteria varies within 4.5–5.2% as a function of p_T^γ and is caused mainly by the anti-track match cut (3%), the correction due to observed data/MC difference from $Z \to ee$ events (1.5–2%), the photon pointing cut uncertainty (2%), the ANN cut (2%) and fitting uncertainty.

We also require at least one hadronic jet found with Run II jet-finding algorithm with cone of $R = 0.7$ that satisfies jet quality criteria. The leading jet (selected after applying jet energy scale corrections) should have $p_T > 15$ GeV and is required to be either in the $|\eta^{jet}| < 0.8$ or the $1.5 < |\eta^{jet}| < 2.5$ pseudorapidity regions. The total leading jet selection efficiency varies from 92% to 99-100% with systematic uncertainties of 5.7% at $p_T^\gamma \simeq 30$ GeV, and decreasing to 2.2% at $p_T^\gamma \geq 200$ GeV.

We select events with the photon candidate and the leading hadronic jet separated in $\eta - \phi$ space by $d\mathcal{R}(\gamma, jet) > 0.7$ with almost 100% efficiency for signal "$\gamma + jet$" events.

B. Estimation of Purity.

A contribution to "$\gamma + jet$" events from di-jet background events occurs when one jet fluctuates to a well-isolated EM clusters. These jets are primarily composed of one or more neutral mesons that decay into photons, and may also be accompanied by other soft hadrons whose energies are deposited in the EM portion of the calorimeter.

Since the signal events cannot be identified on an event-by-event basis, their fraction (purity) $\mathcal{P}$ is determined statistically for a given p_T^γ bin. The photon purity is defined as the ratio

$$\mathcal{P} = \frac{N^\gamma}{N^\gamma + N^{jet}}, \tag{1}$$

where N^γ (N^{jet}) is the number of signal (background) events that passed the selection criteria.

To estimate the background contribution, the ANN output in data is fitted to ANN outputs from simulated photon and QCD EM-jet samples by using the HMCMLL routine [20]. This fitting procedure correctly incorporates the statistical error from both the MC and data inputs. The uncertainty of the measured purity points at low p_T is mostly caused by the low statistics of the simulated QCD jet sample which remains after passing the main selection cuts while for high p_T intervals it is dominated by the data statistics.

The photon fractions determined from HMCMLL were fitted by the function

$$\mathcal{P}_f = 1/(1 + a\ (p_T^\gamma)^b (1 - 2p_T^\gamma/\sqrt{s})^c). \tag{2}$$

We have chosen this form because we expect the data to be a sum of two falling (signal and background) cross sections with their ratio having roughly the form $a(p_T)^b(1-2p_T^\gamma/\sqrt{s})^c$ (compare with formula (1)). Apart from the main fitting function two other functions have been used: $\mathcal{P}_f = 1 - \exp(a + b\ p_T^\gamma)$ and $\mathcal{P}_f = a + b\ \ln(p_T^\gamma) + c\ \ln^2(p_T^\gamma)$. In Fig.4 we plot found purities for all the regions described in the introduction. Each plot contains a default fit with its statistical error as well as the systematic band in uncertainty caused by usage of alternative fitting functions and by variation of the number of bins in the HMCMLL fit. An additional systematic uncertainty in purity was assigned due to the fragmentation model used in the generator PYTHIA [17]. This uncertainty was found to be 5% in purity at $p_T^\gamma \simeq 30$ GeV, 2% at $p_T^\gamma \simeq 50$ GeV, and 1% at $p_T^\gamma \gtrsim 70$ GeV [4].

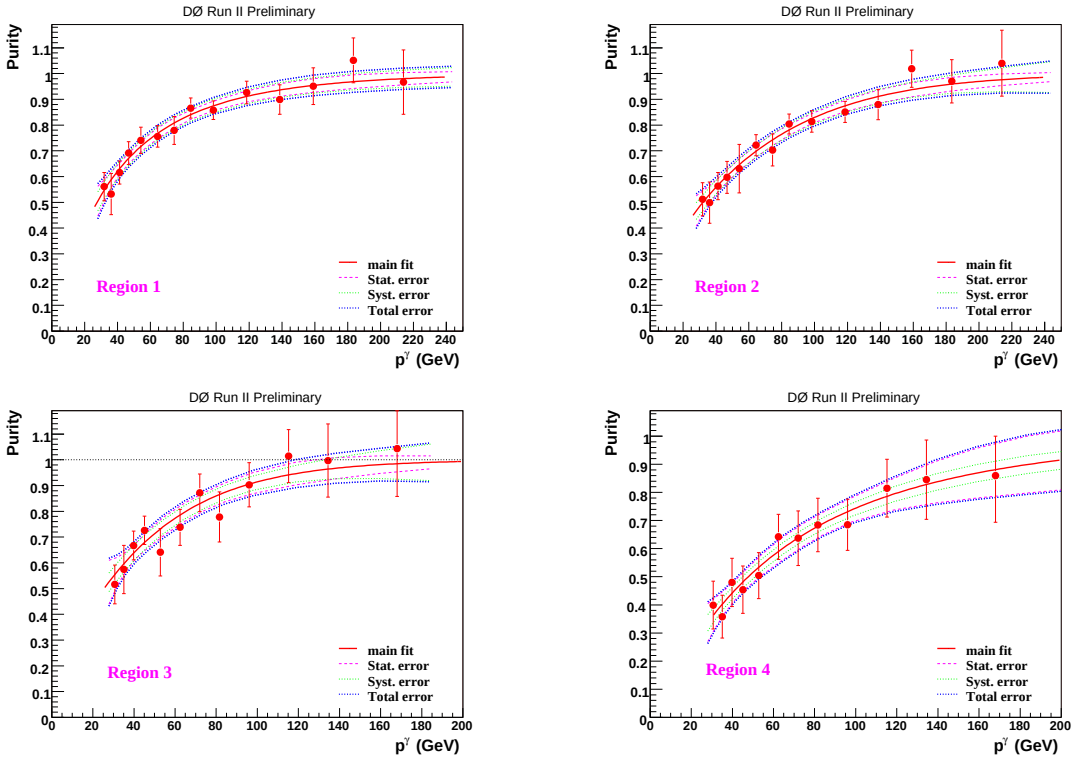

FIG. 4: Dependence of the photon purity on p_T^γ in Region 1 and Region 2. The figure shows default fit (red full line), statistical error from the default fit (purple dashed line), a band in systematic uncertainty (green dotted line) and the total uncertainty (blue dash-dotted line).

C. Unsmearing Corrections.

Unsmearing is correcting a cross section for the smearing which results from the finite resolution of the calorimeter. It is especially important for the case of a steeply falling spectrum. In this study, the unsmearing of the cross section spectra was performed using an analytical method, fitting to the uncorrected cross section a function obtained by the convolution of an initial ansatz (as a physical distribution) and the measured electromagnetic energy resolution function determined from the Z^0 peak. The correction factors were then obtained as a ratio of the unsmeared (physical) to smeared fitted function. The size of correction ranges from 1–5% depending on p_T^γ and the kinematic regions described in the introduction.

III. CALCULATION OF CROSS SECTION AND COMPARISON WITH THEORY.

The triple differential cross section is defined by the relation:

$$\frac{d^3\sigma}{dp_T^\gamma\ d\eta^\gamma\ d\eta^{jet}} = \frac{N\ \mathcal{P}\ f_{unsm}}{L_{int}\ \Delta p_T^\gamma\ \Delta\eta^\gamma\ \Delta\eta^{jet}\ A\ \epsilon_t\ \epsilon_s^\gamma\ \epsilon_s^{jet}} \tag{3}$$

where N is the number of "$\gamma + jet$" candidates in the selected sample, $\mathcal{P}$ is the signal events purity (i.e. their fraction in the selected sample), f_{unsm} is the unsmearing correction factor, L_{int} is the total integrated luminosity, Δp_T^γ, $\Delta\eta^\gamma$ and $\Delta\eta^{jet}$ are the bin sizes in photon transverse momentum, photon and jet pseudorapidities, A is the geometric acceptance, ϵ_t is the trigger efficiency, ϵ_s^γ and ϵ_s^{jet} are efficiencies of the photon and leading jet selection criteria.

The total number of "$\gamma + jet$" events remaining in Regions 1–4 after application of all the selection criteria was about 2.41 million events (∼34.4% in Region 1, 30.2% in Region 2, 20.1% in Region 3 and 13.3% in Region 4) that correspond to $L_{int} = 1.1$ fb^{-1} [21]. These events are used to calculate the cross sections in 15 p_T^γ bins (varied from 30 to 300 GeV) for Regions 1, 2 and in 13 p_T^γ bins (varied from 30 to 200 GeV) for Regions 3, 4. The results of the measurements are shown in Fig. 5 as a function of p_T^γ with the full experimental (systematic ⊕ statistical) errors. The data are plotted at the p_T^γ-weighted average ($\langle p_T^\gamma \rangle$) of the fit function for each bin.

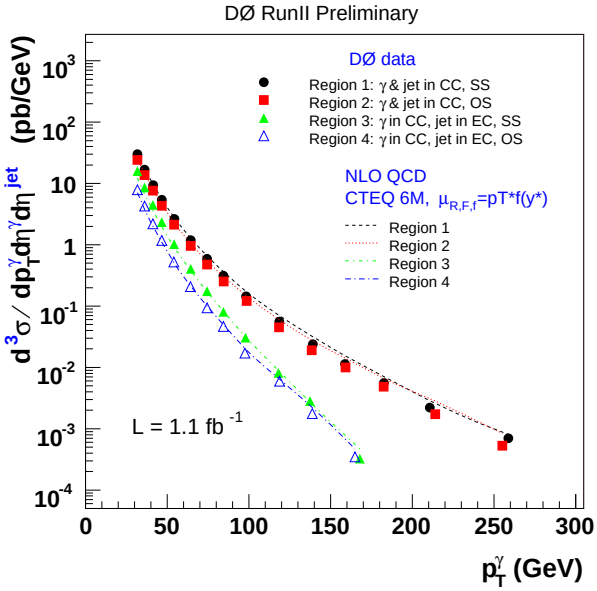

FIG. 5: The differential "$\gamma + jet$" cross sections versus p_T^γ for the four Regions. The full (systematic $\oplus$ statistical) errors are shown. The curves are theoretical NLO QCD predictions from the JETPHOX program [16] with the choice of CTEQ6.1M PDF set [11] and renormalization, factorization and fragmentation scales $\mu_R = \mu_F = \mu_f = p_T^\gamma f(y^\star)$. The data are plotted at the p_T^γ-weighted average of the fit function for each bin.

One can see that in the range of $31.8 < \langle p_T^\gamma \rangle < 258.0$ GeV for Regions 1, 2 the cross sections fall by about 5 orders of magnitude and in the range of $31.8 < \langle p_T^\gamma \rangle < 168.0$ GeV for Regions 3, 4 they change by more than 4 orders of magnitude. Note that the cross sections fall much faster for Regions 3, 4 than for Regions 1, 2.

Statistical errors vary from 0.1% in the first p_T^γ bin to $13-20\%$ in the last bin while systematic errors are within $10-15\%$ (depending on the regions). The main systematic uncertainties are caused by the purity estimate, photon and jet selections and luminosity. Uncertainties of a comparable size are also caused by electromagnetic energy resolution together with the photon p_T correction.

The superimposed theoretical curve corresponds to the QCD NLO predictions based on the JETPHOX program [12, 16] with the choice of CTEQ6.1M set of parton distribution functions (PDF) [11] and set of fragmentation functions [22].

The theoretical predictions presented in Fig. 5 correspond to the choice of renormalization, factorization and fragmentation scales chosen as $\mu_R = \mu_F = \mu_f = p_T^\gamma f(y^\star)$ with $f(y^\star) = ([1+exp(-2|y^\star|)]/2)^{1/2}$ and $y^\star = 0.5(\eta^\gamma - \eta^{jet})$ [23] [27].

The ratio of the measured cross section to the NLO QCD predictions [16] calculated with the CTEQ6.1M PDF set are presented in Figs. 6, 7 for all kinematic regions. Ratios of the nominal theory predictions [16] (with the PDF set corresponding to the best fit and all scales chosen as $\mu_{R,F,f} = p_T^\gamma f(y^\star)$) to the predictions with $\mu_{R,F,f} = 0.5 p_T^\gamma f(y^\star)$ and $2p_T^\gamma f(y^\star)$ are shown on the plots by two dashed lines. They differ by 9–11% for Regions 1–3 and 18–20% for Region 4. Only the statistical uncertainties are shown in the data points. The p_T dependent systematic uncertainties are shown on the plots separately by a shaded region. Additional p_T independent uncertainties from the luminosity measurement (6%), photon selection efficiency (4.6%), acceptance (1.5%) and unsmearing (1%) lead to 7.8% overall normalization uncertainty.

In order to reduce the systematic uncertainty of measured cross sections in the four kinematic regions, we have also calculated ratios of the cross sections between different regions. Namely, cases with cross section ratios between Regions 1 and 2, 1 and 3, 2 and 3, and 3 and 4 were considered. The calculated ratios with experimental uncertainties are presented in Figs. 8 and 9. Since in all the four regions we use only "central" photons, most systematic uncertainties related with their identification are canceled in the ratios. We assume that the only systematic uncertainties that survive in the ratio are related to the "$\gamma + jet$" event purity (since it differs a little between the four regions) and the jet selection efficiency when we calculate ratios with the central leading jet in one region and the forward leading jet in another region. The overall experimental uncertainty estimated in such a way is about 3.5–9% for $44 < p_T^\gamma < 110$ GeV and becomes larger for smaller p_T^γ (due to systematics) and larger p_T^γ (due to statistics) as shown on the plots of Figs. 8 and 9 by the full vertical error lines. The internal error line indicates just the statistical uncertainty. It is obtained by summing the statistical uncertainties for the different regions in quadrature.

As we see from Figs. 6 and 7, the results of the measurements show a deviation from theory predictions for $p_T^\gamma > 100$ GeV for the two kinematic regions with the photon and jet both located in the central pseudorapidity regions. A deviation is also seen for $p_T^\gamma < 50$ GeV for the kinematic region with the photon in the central and the jet in the forward pseudorapidity regions with same sign of their pseudorapidities. Note that the shape of the data-to-theory ratios with the photon and jet both in the central pseudorapidity regions (their cross sections are much larger than those with forward jets, see Fig. 5) is similar to a structure previously observed by the UA2 [24], CDF [25] and DØ [4] experiments.

The shapes of the measured cross section ratios in data, in general, are qualitatively reproduced by the theory but we observe a quantitative disagreement for some kinematic regions even after accounting for the overall (experimental and theoretical scale) uncertainty. It is especially noticeable for the cross section ratios between Regions 1 and 3 as well as Regions 2 and 3.

We are very thankful to P. Aurenche, M. Fontannaz, J.P. Guillet, and M. Werlen for providing JETPHOX package, useful discussions and their assistance with theoretical calculations.

We thank the staffs at Fermilab and collaborating institutions, and acknowledge support from the DOE and NSF (USA); CEA and CNRS/IN2P3 (France); FASI, Rosatom and RFBR (Russia); CAPES, CNPq, FAPERJ, FAPESP and FUNDUNESP (Brazil); DAE and DST (India); Colciencias (Colombia); CONACyT (Mexico); KRF (Korea); CONICET and UBACyT (Argentina); FOM (The Netherlands); PPARC (United Kingdom); MSMT (Czech Republic); CRC Program, CFI, NSERC and WestGrid Project (Canada); BMBF and DFG (Germany); SFI (Ireland); Research Corporation, Alexander von Humboldt Foundation, and the Marie Curie Program.

---

[1] DØ Collaboration, B. Abbott *et al.* Phys.Rev. **D64** (2001)032003.
[2] DØ Collaboration, B. Abbott *et al.* Phys.Rev.Lett. **84** (2000)2786.
DØ Collaboration, V. Abazov *et al.* Phys.Rev.Lett. **87** (2001)2518.
[3] DØ Collaboration, V. Abazov *et al.*, Phys.Rev.Lett. **94** (2005)221801.
DØ Collaboration, V. Abazov *et al.*, DØ Conference note 5087, hep-ex/0609026.
[4] DØ Collaboration, V. Abazov *et al.*, Phys.Lett. **B639**, (2006)151. Erratum to this paper is in preparation.
[5] D.V. Bandurin and N.B. Skachkov, Phys.Part.Nucl.**35** (2004)66.
[6] E.L. Berger and J. Qiu, Phys.Rev. **D44** (1991)2002.
[7] P. Aurenche, R. Baier, M. Fontannaz, J.F. Owens and M. Werlen, Phys.Rev. **D39** (1989)3275.
[8] W. Vogelsang and A. Vogt, Nucl.Phys. **B453** (1995)334.
[9] A.D. Martin *et al.*, Eur.Phys.J. **C4** (1998)463.
[10] Wu-Ki Tung, hep-ph/0409145.
[11] J. Pumplin *et al.*, JHEP **0207** (2002)012; D. Stump *et al.*, JHEP **0310** (2003)046.
[12] P. Aurenche, R. Baier, M. Fontannaz and D. Schiff, Nucl.Phys. **B297** (1988)661;
F. Aversa, P. Chiappetta, M. Greco and J.Ph. Guillet, Nucl.Phys. **B327** (1989)105;
S. Catani, M. Fontannaz, J.Ph. Guillet and E. Pilon, Preprint LAPTH-907/02, JHEP **0205** (2002)028.
[13] ISR–AFS Collaboration, T. Akesson *et al.*, Zeit.Phys. **C34** (1987)293.
[14] UA2 Collaboration, J. Alitti *et al.*, Phys.Lett. **B229** (1993)174.
[15] CDF Collaboration, F. Abe *et al.*, Phys.Rev. **D57** (1998)67.
[16] JETPHOX package, http://wwwlapp.in2p3.fr/lapth/PHOX_FAMILY/main.html. See also [12] for the list of contributing authors and related references.
[17] T. Sjostrand, Comp.Phys.Comm. **82** (1995)74.
[18] DØ Collaboration, V. Abazov *et al.*, Nucl.Instrum.Methods, Phys.Res., A**565** (2006)463.
[19] C. Peterson, T. Rognvaldsson and L. Lonnblad, Comp.Phys.Comm. **81** (1994)15.
[20] R. Barlow, C. Beeston, Comp.Phys.Comm. **77** (1993)219. See also p.120-131 of HBOOK manual.
[21] T. Andeen *at al.*, FERMILAB-TM-2365-E (2006), in preparation.
[22] L. Bourhis, M. Fontannaz and J.Ph. Guillet, Eur.Phys.J. **C2** (1998)529.
[23] This scale choice is suggested by Jean-Philippe Guillet and Michel Fontannaz.
[24] UA2 Collaboration, J. Alitti *et al.*, Phys.Lett. **B263** (1991)544.
[25] CDF Collaboration, D. Acosta *et al.*, Phys.Rev. **D65** (2002)112003.
[26] Pseudorapidity is defined as $\eta = -\ln\tan(\theta/2)$, where θ is the polar angle with respect to the proton beam direction.
[27] Note that for $|y^\star| \simeq 0$ (approximately corresponding to Region 1), this scale coincides with p_T^γ, while for $|y^\star| \simeq 1$ (more or less corresponding to Region 2), the scale is $0.84 p_T^\gamma$ and for $|y^\star| \simeq 1.5$ (2) ($\approx$ corresponds to Region 3 (4)), scale is 0.78 (0.71)p_T^γ.

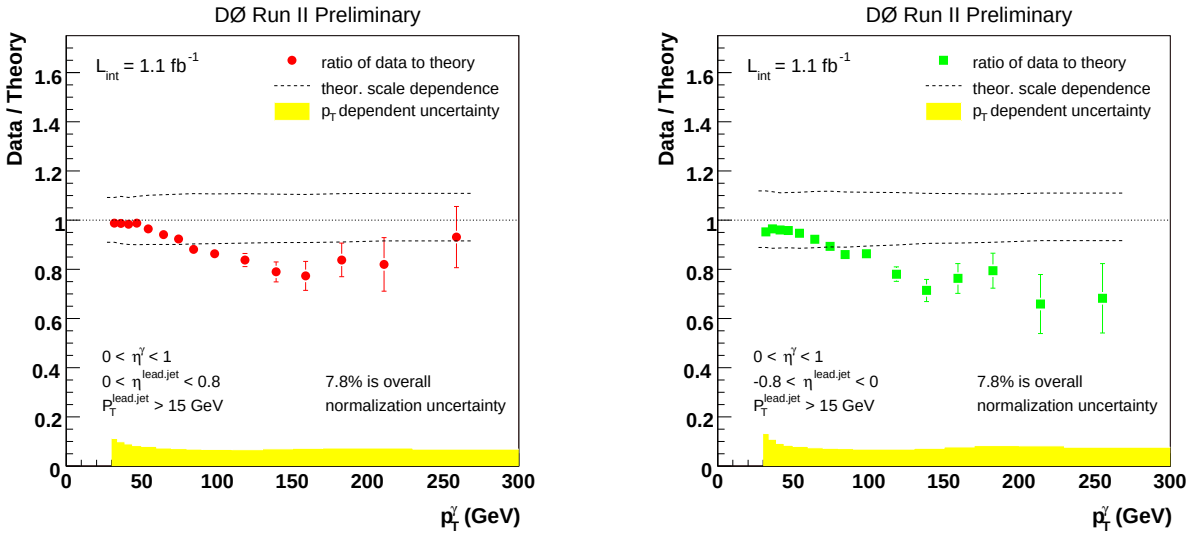

FIG. 6: Left plot: The ratio of the measured cross section in *Region 1* to the NLO QCD predictions done with [16] with the CTEQ6.1M PDF set and all three scales $\mu_{R,F,f} = p_T^{\gamma} f(y^{\star})$. The two dashed lines represents the change in the cross section when varying the theoretical scales by factor of two. Right plot: Same as in the description to the left plot but for *Region 2*. Just statistical uncertainties are shown in the data points. The total p_T dependent uncertainties are shown by the shaded region in the bottom part of each plot.

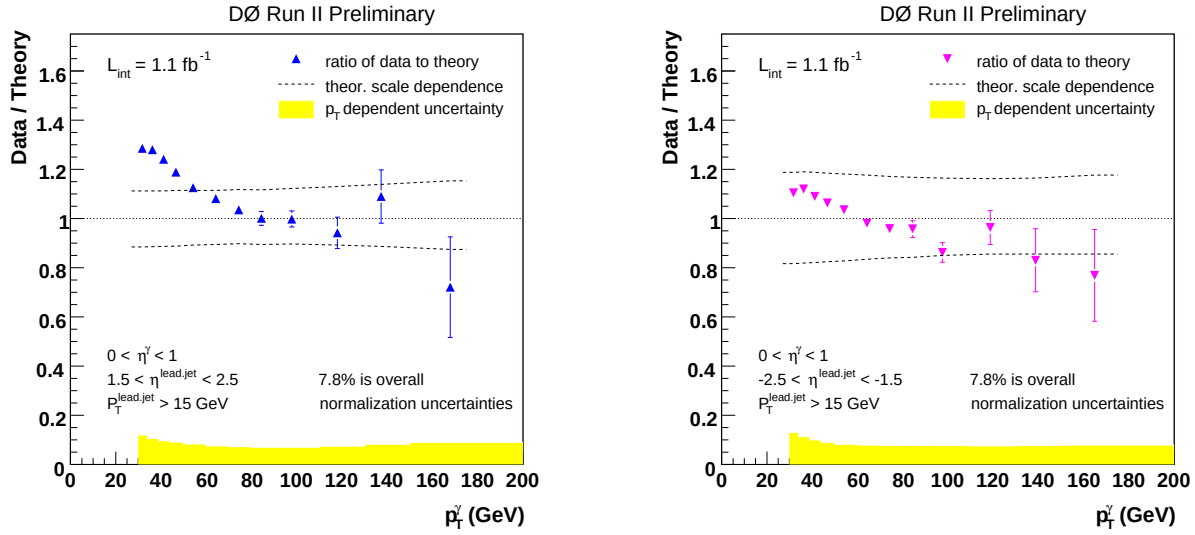

FIG. 7: Left plot: Same as Figure 6 but for *Region 3*. Right plot: Same as Figure 6 but for *Region 4*.

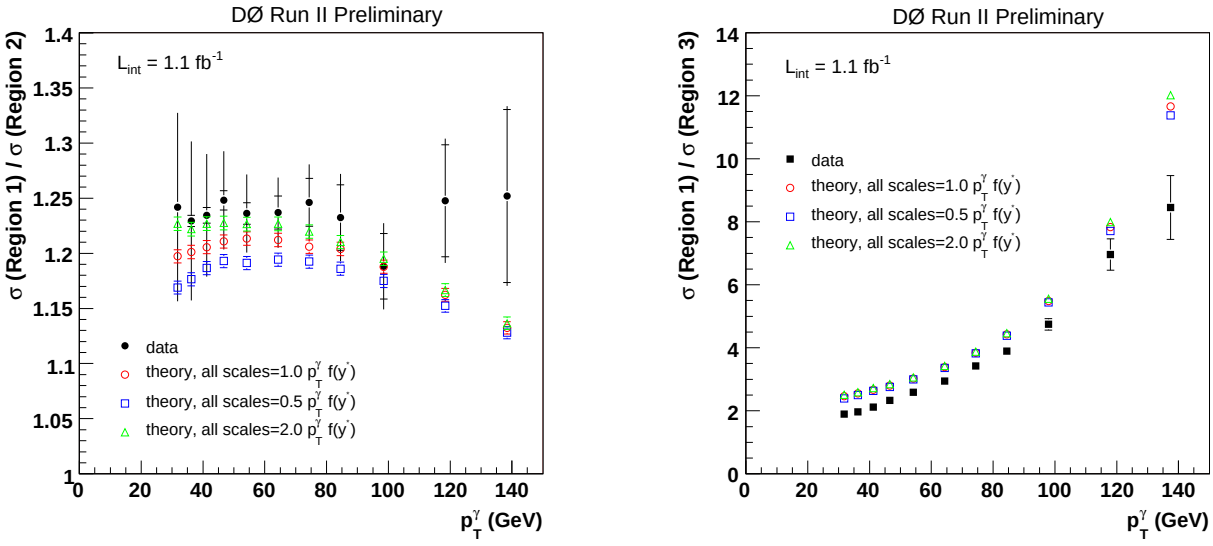

FIG. 8: Left plot: the ratio of the differential cross sections in *Region 1* to *Region 2*. Right plot: the ratio of the differential cross sections in *Region 1* to *Region 3*. The full vertical error lines in data points (•) correspond to the overall uncertainty while the internal line indicates just the statistical uncertainty. Theoretical predictions are calculated with three different set of scales: $\mu_{R,F,f} = p_T^\gamma f(y^\star)$, $0.5 p_T^\gamma f(y^\star)$ and $2.0 p_T^\gamma f(y^\star)$ (three open symbols).

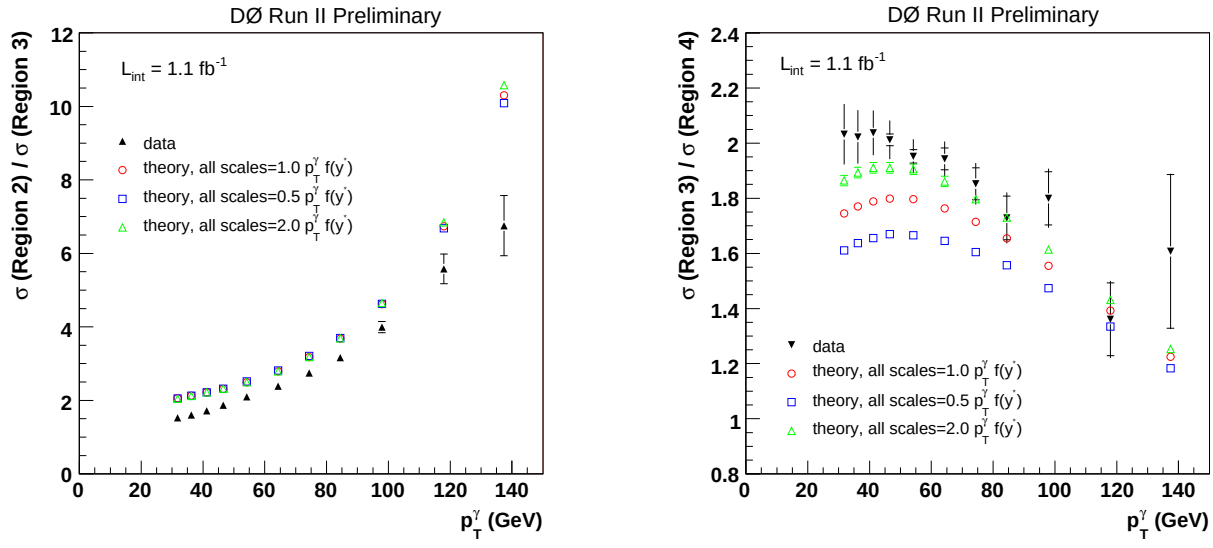

FIG. 9: Left plot: The ratio of the differential cross sections in *Region 2* to *Region 3*. Right plot: The ratio of the differential cross sections in *Region 3* to *Region 4*. The full vertical error lines in data points (•) correspond to the overall uncertainty while the internal line indicates just the statistical uncertainty. Theoretical predictions are calculated with three different set of scales: $\mu_{R,F,f} = p_T^\gamma f(y^\star)$, $0.5 p_T^\gamma f(y^\star)$ and $2.0 p_T^\gamma f(y^\star)$ (three open symbols).